



Article

Improved Estimation of the Open Boundary Conditions in Tidal Models Using Trigonometric Polynomials Fitting Scheme

Shengyi Jiao ^{1,2}, Yibo Zhang ^{1,2}, Haidong Pan ^{3,4,*} and Xianqing Lv ^{1,2}

- ¹ Frontier Science Center for Deep Ocean Multispheres and Earth System (FDOMES), Ocean University of China, Qingdao 266100, China
- ² Laboratory for Regional Oceanography and Numerical Modeling, Pilot National Laboratory for Marine Science and Technology, Qingdao 266237, China
- ³ First Institute of Oceanography, and Key Laboratory of Marine Science and Numerical Modeling, Ministry of Natural Resources, Qingdao 266061, China
- ⁴ Shandong Key Laboratory of Marine Science and Numerical Modeling, Qingdao 266061, China
- * Correspondence: panhaidong@fio.org.cn

Abstract: Tidal open boundary conditions (OBCs) of the M_2 tidal constituent in the Bohai and Yellow Seas (BYS) are estimated via the assimilation of multi-satellite altimeter data to optimize regional tidal numerical simulation. A two-dimensional adjoint assimilation model is used for tidal numerical simulation and, as an improvement, trigonometric polynomials fitting (TPF) is applied in the inversion of OBCs. It is assumed that the linearized amplitudes/phases in the open boundary are spatially varying and can be represented by nonlinear functions. Based on the discrete Fourier series, taking the trigonometric function as the basis function, the spatially varying OBCs are constructed by selecting the maximum truncation period. The independent points scheme used in previous studies was also compared in the experiments. Twin experiments show that the errors of simulations with TPF are the smallest in different schemes, and their results show the highest correlation with observations while maintaining the best performance in terms of observation errors. The mean absolute errors (MAEs) in amplitude/phase between the simulated results using estimated OBCs and the satellite altimeter records are 2.82 cm and 2.26°, respectively.

Keywords: inverse methods; open boundary conditions; adjoint method; satellite altimeter data; trigonometric polynomials fitting; tidal modeling



Citation: Jiao, S.; Zhang, Y.; Pan, H.; Lv, X. Improved Estimation of the Open Boundary Conditions in Tidal Models Using Trigonometric Polynomials Fitting Scheme. *Remote Sens.* **2023**, *15*, 480. <https://doi.org/10.3390/rs15020480>

Academic Editor: Xiaoli Deng

Received: 7 December 2022

Revised: 7 January 2023

Accepted: 10 January 2023

Published: 13 January 2023



Copyright: © 2023 by the authors. Licensee MDPI, Basel, Switzerland. This article is an open access article distributed under the terms and conditions of the Creative Commons Attribution (CC BY) license (<https://creativecommons.org/licenses/by/4.0/>).

1. Introduction

Tides are one of the earliest aspects of oceanography to be recognized and applied in human activities [1]. Tides, as a basic motion of seawater, are of great significance to research on water mass, ocean currents, storm surges and other ocean phenomena [2]. The study of such seawater motions remains an important part of oceanography, with significant implications for coastal engineering and the exploitation of marine resources, especially in shallow seas. The Bohai and Yellow Seas (BYS) are marginal seas adjacent to China, where tides and tidal currents are rather strong and complicated. Based on observations and numerical models, the cotidal charts of the BYS have been constructed, revealing the basic characteristics of the main tidal constituents in the BYS [3–6], though quantitative improvement is still necessary.

The regional ocean models play an irreplaceable role in the investigation of tidal characteristics for the marginal seas. Numerical models of coastal ocean regions inevitably involve the treatment of open boundaries and, therefore, appropriate open boundary conditions (OBCs) must be applied [7]. In regional ocean models, OBCs are essential for accurate simulation of tidal processes, and solutions in model interior are determined by the OBCs [8]. In general, OBCs are obtained by interpolating the available observations near the open boundaries or deriving from larger scale models (e.g., the widely used TPXO

tidal model data) through a nested grid approach [9,10]. In the case of lacking observations near the open boundary, significant uncertainties are introduced into the model by such interpolated or extrapolated boundary values [11]. In practice, the model data may be inapplicable in terms of resolution and accuracy in shallow waters [12], which means that manual adjustments need to be made empirically to obtain satisfactory simulation results [13]. Adjoint method is widely implemented as a more advanced and powerful tool for the estimation of OBCs and other tidal parameters [14–18].

Obtaining OBCs by adjoint methods also requires the support of observations. Tide gauge data are commonly used for tide studies; however, tide gauges are mainly located in shallow water, with a small number and uneven distribution [19], which poses a challenge to the accuracy of regional tidal numerical research. The development of remote sensing technology has made up for this shortcoming, and satellite altimeter data cover a much larger area, including the open ocean, providing a great help to better study ocean tides [20,21]. In recent years, great development and progress has been made in altimeter instrumentation, processing algorithms and corrections, and products represented by X-TRACK have significantly improved the accuracy of altimeter data in coastal areas [22]. The application of satellite altimeter data and products improves the inversion of tidal parameters by the adjoint method.

Satellite altimetry inevitably has some shortcomings. Different from the continuous and high-frequency sampling of tide gauge, the satellite altimeter data are limited by the orbit design, and the sampling rate is insufficient for ocean tides. Too long a sampling period at the same location will lead to tidal aliasing, which is not conducive to the study of ocean tides [23]. The accuracy of measured altimeter data can be affected as the satellite approaches the coasts due to the contamination of signal by land [24], which will lead to greater error in the altimeter data near the coast compared with that in the deep sea. In order to analyze tidal residuals in satellite data, gravity models of nontidal variability are required [25], but there are certain technical defects in gravity recovery and climate experiments (GRACE) and gravity models [26]. Accurate simulation of ocean tides serves as a correction for spaceborne measurements; it can be directly used for satellite altimetry data correction or indirectly used as GRACE or gravity field modeling [23]. Therefore, more accurate numerical simulation of ocean tides also plays a significant role in the development of satellite altimetry.

In addition, the OBCs inversion with the adjoint method has been continuously optimized. In the original research, all points on the boundary were set as control parameters, which easily caused the ill-posedness of the inverse problem [27–29]. For this problem, the independent points (IPs) scheme was proposed for optimization. With the help of IPs scheme, Lu and Zhang [30] developed a two-dimensional (2D) tidal model and successfully inverted the bottom friction coefficients (BFCs). Since the interpolation is a core part of IPs scheme, the parameter settings of IPs selection and influence radius are constantly explored. Using a 2D tidal model, Cao et al. [31] investigated the effect of different IP strategies on the inversion simulation results of OBCs in the BYS, indicating that using only two IPs can yield better simulated results. The IPs scheme has been applied to estimate OBCs, BFCs and other parameters in tide and internal tidal models [32–35]. In the above studies, linear interpolation was used in the IPs scheme, which would lead to non-smooth parameters of inversion. As an improvement, Pan et al. [36] proposed to replace the Cressman interpolation (CI) with the spline interpolation (SI) to make inversed OBCs smoother and reduce the error of simulation results. Since then, IPs combined with SI have been continuously explored in the inversion of tidal parameters [37,38].

However, the location selection of IPs and influence radius are always unavoidable for IPs scheme when the method is applied to more general and open areas, a large number of sensitive experiments are required to obtain the best simulation results [32]. For parameter estimation problems, it is of great importance to reduce the number of spatially varying control parameters due to the ill-posedness of the inverse problem [35]. In this paper, trigonometric polynomials fitting (TPF) scheme is proposed to express the spatially

varying OBCs and improve the estimation of OBCs in a 2D tidal model. The components of OBCs are expressed as a discrete Fourier series, and a finite number of trigonometric polynomials are used to construct OBCs, which reduces the number of control parameters. The BYS are selected as the computation domain; the more accurate and appropriate OBCs are estimated for regional tidal models by assimilating observations to optimize the coefficients of polynomials. The satellite altimeter data used for assimilation are also updated. Compared with previous studies, the data cover a wider time range and have higher accuracy, which can achieve more accurate tidal simulation. The IPs scheme is used as a comparison in the following experiments. Meanwhile, OBCs derived from data of ocean tidal models are used to perform numerical simulations to validate the inversion effect of TPF scheme.

This paper is organized as follows: the tidal model and derivation of the correction of parameters are shown in Section 2. In Section 3, twin experiments (TEs) are conducted to examine the feasibility and accuracy of TPF. In Section 4, practical experiment (PE) is carried out in the BYS. The conclusion and summary are presented in Section 5.

2. Method and Materials

2.1. Forward Model

Considering the variation in Coriolis force with latitude, the depth average 2D equations under the Cartesian co-ordinate system are expressed as follows:

$$\frac{\partial \zeta}{\partial t} + \frac{\partial[(h + \zeta)u]}{\partial x} + \frac{\partial[(h + \zeta)v]}{\partial y} = 0 \quad (1)$$

$$\frac{\partial u}{\partial t} + u \frac{\partial u}{\partial x} + v \frac{\partial u}{\partial y} - fv + \frac{Ku\sqrt{u^2 + v^2}}{h + \zeta} - A \left(\frac{\partial^2 u}{\partial x^2} + \frac{\partial^2 u}{\partial y^2} \right) + g \frac{\partial(\zeta - \bar{\zeta})}{\partial x} = 0 \quad (2)$$

$$\frac{\partial v}{\partial t} + u \frac{\partial v}{\partial x} + v \frac{\partial v}{\partial y} + fu + \frac{Kv\sqrt{u^2 + v^2}}{h + \zeta} - A \left(\frac{\partial^2 v}{\partial x^2} + \frac{\partial^2 v}{\partial y^2} \right) + g \frac{\partial(\zeta - \bar{\zeta})}{\partial y} = 0 \quad (3)$$

where t is time; h is the bathymetry; ζ is the water elevation above the undisturbed sea level; $\bar{\zeta}$ is the water elevation caused by tide-generating force; u and v are the depth-averaged velocity components eastward and northward, respectively; f is the Coriolis parameter; g is a constant (9.8 m/s^2); A is the eddy viscosity coefficient; and K is the BFCs.

The initial conditions are set to $\zeta = u = v = 0$. At the closed boundaries, the normal velocity is 0.

During the modeling of tidal processes, the tidal dynamic information at the open boundaries for each tidal constituent must be provided, which have a significant impact on simulation results [6,15]. The M_2 tidal constituent is selected as the research constituent in this paper, and the spatiotemporal varying water elevations along the open boundaries (or OBCs) are given by:

$$\zeta_l^j = \alpha(l) \cos(\omega j \Delta t) + \beta(l) \sin(\omega j \Delta t) \quad (4)$$

where α and β are the Fourier coefficients (FCs) of OBCs, l is the grid index at the open boundaries, j is time step and ω denotes the angular frequency of the M_2 tidal constituent.

The water elevation caused by tide-generating force term can be expressed as:

$$\bar{\zeta}^j = \bar{H} \cos(\omega j \Delta t + c\phi) \quad (5)$$

where ϕ is the longitude and, for semi-diurnal tidal constituents, $c = 2$. According to Wahr [39], \bar{H} of the M_2 constituent is described as: $\bar{H} = 0.168 \cos^2 \varphi$, and φ is the latitude.

The simulation domain covers $117^\circ 30' \text{E} \sim 126^\circ 40' \text{E}$, $34^\circ \text{N} \sim 41^\circ \text{N}$, with $1/6^\circ$ horizontal resolution. The model adopts the Arakawa C grid. As the research object is the M_2 tidal constituent, the time step interval is set to be 372.618 s, $1/120$ of the period of the M_2 tidal

constituent. The bathymetry of the BYS and the locations of observations are shown in Figure 1.

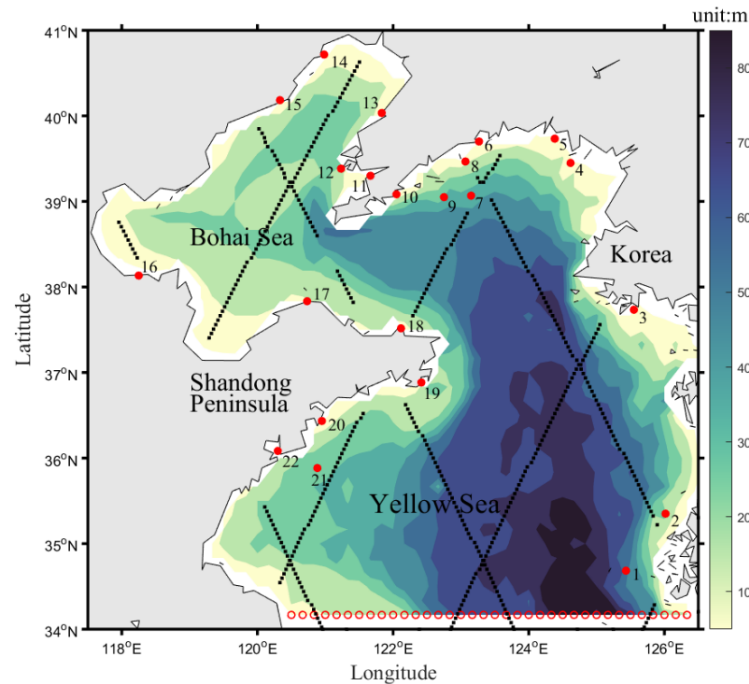


Figure 1. The bathymetry of the BYS, the location of open boundaries (red circles), the altimeter data (black points) and the tidal gauges (red points).

2.2. Adjoint Model

To estimate the difference in water elevation between simulations and observations, a cost function is defined according to the adjoint method [30,40]:

$$J(\zeta) = \frac{1}{2} K_{\zeta} \int_{\Sigma} (\zeta - \hat{\zeta})^2 d\sigma \tag{6}$$

where K_{ζ} is a constant (here, $K_{\zeta} = 1$), Σ denotes the collection of observation points, and ζ and $\hat{\zeta}$ are simulated results and observations, respectively. Then, the Lagrangian function is defined as:

$$\begin{aligned} L(\zeta, u, v, \lambda, \mu, \nu, a_k, b_k, p_k, q_k) = & J(\zeta) + \int_{\Sigma} \left\langle \lambda \left\{ \frac{\partial \zeta}{\partial t} + \frac{\partial[(h+\zeta)u]}{\partial x} + \frac{\partial[(h+\zeta)v]}{\partial y} \right\} \right. \\ & + \mu \left\{ \frac{\partial u}{\partial t} + u \frac{\partial u}{\partial x} + v \frac{\partial u}{\partial y} - fv + \frac{Ku\sqrt{u^2+v^2}}{h+\zeta} - A \left(\frac{\partial^2 u}{\partial x^2} + \frac{\partial^2 u}{\partial y^2} \right) + g \frac{\partial(\zeta-\bar{\zeta})}{\partial x} \right\} \\ & \left. + \nu \left\{ \frac{\partial v}{\partial t} + u \frac{\partial v}{\partial x} + v \frac{\partial v}{\partial y} + fu + \frac{Kv\sqrt{u^2+v^2}}{h+\zeta} - A \left(\frac{\partial^2 v}{\partial x^2} + \frac{\partial^2 v}{\partial y^2} \right) + g \frac{\partial(\zeta-\bar{\zeta})}{\partial y} \right\} \right\rangle d\sigma \end{aligned} \tag{7}$$

where λ , μ and ν are the adjoint variables of ζ , u and v , respectively. According to the theory of Lagrangian multiplier method, to minimize the cost function, the adjoint model can be described as:

$$\frac{\partial L}{\partial \zeta} = 0, \quad \frac{\partial L}{\partial u} = 0, \quad \frac{\partial L}{\partial v} = 0 \tag{8}$$

2.3. Parameter Optimization

In the TPF scheme, control parameters α and β are subjected to discrete Fourier transform, and then constructed from a finite number of trigonometric polynomials, which can be expressed as:

$$\alpha(l) = \sum_{k=0}^N [a_k \cos(\omega_l k l) + b_k \sin(\omega_l k l)] \tag{9}$$

$$\beta(l) = \sum_{k=0}^N [p_k \cos(\omega_l k l) + q_k \sin(\omega_l k l)] \tag{10}$$

where $\{a_k, b_k, p_k, q_k : k = 1, \dots, N\}$ are the coefficients of polynomials, which are optimized directly as control parameters in the subsequent experiments, and then form FCs of estimated OBCs. $\omega_l = 2\pi/L_b$ denotes the frequency of the trig functions, and L_b is the number of grid points along the open boundary. N is the maximum truncation period (MTP). In the experiments, FCs for OBCs can be constructed by selecting different N .

The gradient expression of control parameters can be obtained by the following equations:

$$\frac{\partial L}{\partial a_k} = 0, \quad \frac{\partial L}{\partial b_k} = 0, \quad \frac{\partial L}{\partial p_k} = 0, \quad \frac{\partial L}{\partial q_k} = 0 \tag{11}$$

According to Equation (11) and the steepest decent method, the correction of control parameters in the OBCs can be expressed:

$$a'_k = a_k - K_c \sum_{j=1}^M \sum_{l=1}^{L_b} T_l^j \cos(\omega_j \Delta t) \cos(\omega_l k l) \tag{12}$$

$$b'_k = b_k - K_c \sum_{j=1}^M \sum_{l=1}^{L_b} T_l^j \cos(\omega_j \Delta t) \sin(\omega_l k l) \tag{13}$$

$$p'_k = p_k - K_c \sum_{j=1}^M \sum_{l=1}^{L_b} T_l^j \sin(\omega_j \Delta t) \cos(\omega_l k l) \tag{14}$$

$$q'_k = q_k - K_c \sum_{j=1}^M \sum_{l=1}^{L_b} T_l^j \sin(\omega_j \Delta t) \sin(\omega_l k l) \tag{15}$$

where a'_k, b'_k, p'_k, q'_k are corrected coefficients of trig functions with the period of k , M is the total number of time steps in a tidal cycle and K_c is the weight coefficient of optimization, which is related to the gradient and generally decreases with the steps of iterations. T_l^j varies with specific conditions:

$$\begin{aligned} T_l^j &= -g\mu_{m_l, n_l}^j / \Delta x, \text{ if } (m_l, n_l) \text{ is on a left open boundary;} \\ T_l^j &= -g\mu_{m_l-1, n_l}^j / \Delta x, \text{ if } (m_l, n_l) \text{ is on a right open boundary;} \\ T_l^j &= -g\nu_{m_l, n_l}^j / \Delta y, \text{ if } (m_l, n_l) \text{ is on a lower open boundary;} \\ T_l^j &= -g\nu_{m_l, n_l-1}^j / \Delta y, \text{ if } (m_l, n_l) \text{ is on an upper open boundary.} \end{aligned}$$

2.4. Data and Sources

M_2 harmonic constants used for assimilation were derived from T/P-Jason (TOPEX/Poseidon, Jason-1, Jason-2 and Jason-3) satellite altimeter data processed by X-TRACK software. With the processing of X-TRACK software, the outlines in altimetric corrections are more efficiently detected, the missing or rejected correction values are better reconstructed, and the correlation between near-shore altimetry sea level anomaly and tidal gauge records is substantially increased [22].

The observation data of T/P-Jason satellite altimeter processed by X-TRACK were provided by AVISO, including data from the above four satellite altimeters from March 1993 to May 2020. These satellites have the same tracks (Figure 1 points) and the sampling interval is 9.915642 days. Harmonic constants of the M_2 constituent along the T/P-Jason altimeter tracks are shown in Figure 2. The bathymetry was provided by National Marine Data and Information Service (NMDIS).

In this study, the TPX09 with $1/6^\circ$ horizontal resolution [10,41], the Finite Element Solutions 2014 (FES2014) model with $1/16^\circ$ horizontal resolution [42], the EOT20 with $1/8^\circ$ horizontal resolution [43], the National Astronomical Observatory 99b (NAO.99b) model with $1/2^\circ$ horizontal resolution [44] and a purely empirical ocean tidal model OSU12 with $1/4^\circ$ horizontal resolution are taken into consideration. Stammer et al. [25] assessed the accuracy of global barotropic tidal models using bottom pressure data, coastal tide gauges, satellite altimeter and other data, and their study showed that TPX08 (the previous version

of TPX09) and FES2012 (the previous version of FES2014) appear to perform better in the shelf seas. Hart-Davis et al. [43] presented a comparison of the results of six global tidal models, including EOT20 and FES2014, and the EOT20 had better performance, especially in the coastal region.

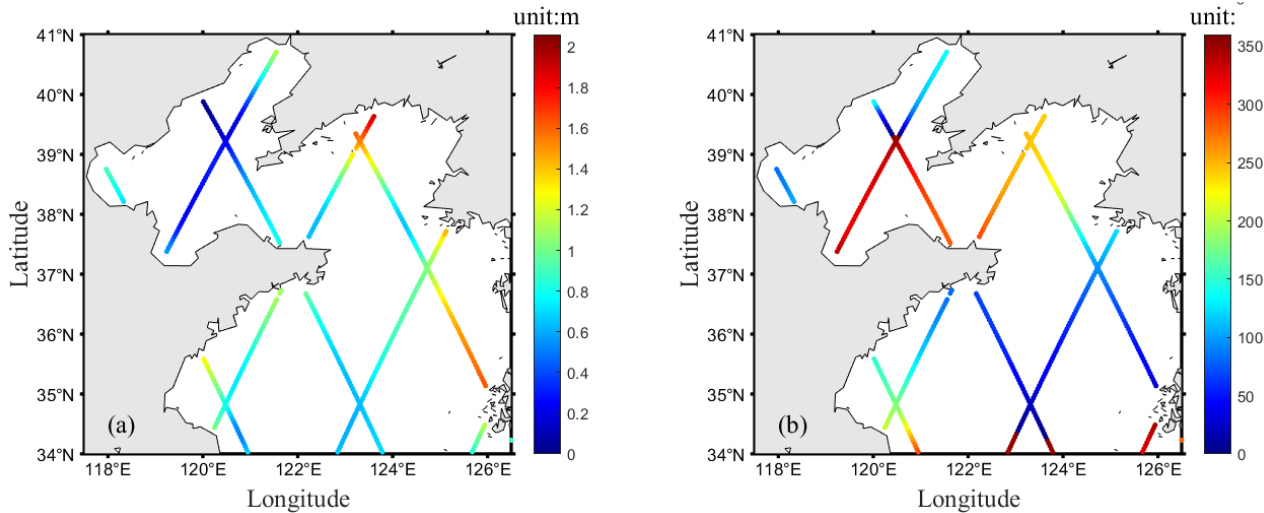


Figure 2. The amplitude (a) and phase (b) of M_2 constituent along T/P-Jason altimeter tracks in the BYS.

3. Twin Experiments

In this section, eight TEs are conducted to evaluate the feasibility and accuracy of the model and TPF scheme. Referring to Lu and Zhang [38], the spatially varying BFCs (Figure 3) are estimated by adjoint assimilation. The estimated BFCs in the major bays of the BYS are relatively large, which may be related to the local topography or formation of drag [45–47]. The BFCs remain unchanged in the experiments and the eddy viscosity coefficient keeps constant during experiments.

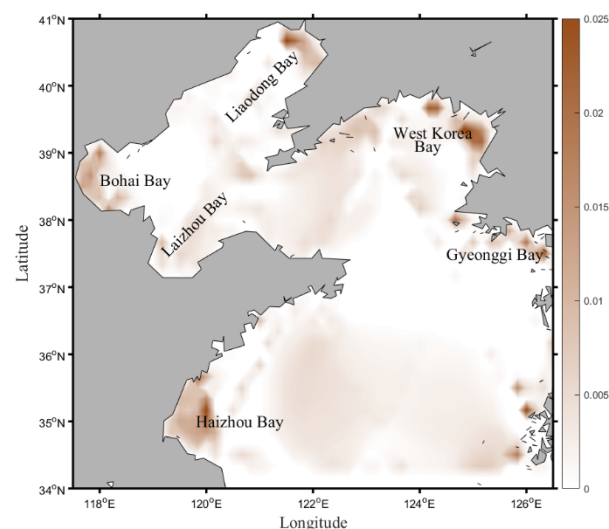


Figure 3. The distribution of estimated BFCs in the BYS.

3.1. Inversion Process

The process of TEs is listed as follows:

Step 1: The forward model is run with prescribed OBCs and BFCs (Figure 3), and the simulated results on T/P-Jason altimeter tracks are chosen as “observations”.

Step 2: The FCs (the initial taken as zero here) of OBCs are used for running the forward model to obtain simulated water elevations.

Step 3: The difference in water elevations between simulated results from step 2 and “observations” in step 1 is used as the external drive to calculate the cost function.

Step 4: The gradients of the control parameters (a_k, b_k, p_k, q_k) are calculated by Equation (11), and then the control parameters are optimized by Equations (12)–(15).

Step 5: Optimized control parameters are assigned to new FCs of OBCs.

Steps 2–5 are repeated and the difference in water elevation simulation results and “observations” decreases. When a convergence criterion is met or the number of iteration steps reaches the specified number, the process of inversion terminates.

3.2. TEs Setting

In TEs 1–4, four given FCs α are inverted, while β is set to be zero and does not participate in the inversion. Previous studies have shown that IPs schemes work best when the radius of influence is equal to the distance between IPs [31,36]. TEs setting is determined according to the basic research and preliminary experiments. The inversion process terminates when the number of iteration steps reaches 100. Several preliminary experiments were conducted to determine the number of IPs in IPs schemes and the maximum number of cycles in TPF scheme in different experiments. In TEs 1–4, for CI and SI schemes, five independent points are selected uniformly, and the MTP in TPF scheme is set to 1. The given and inverted FCs α are displayed in Figure 4.

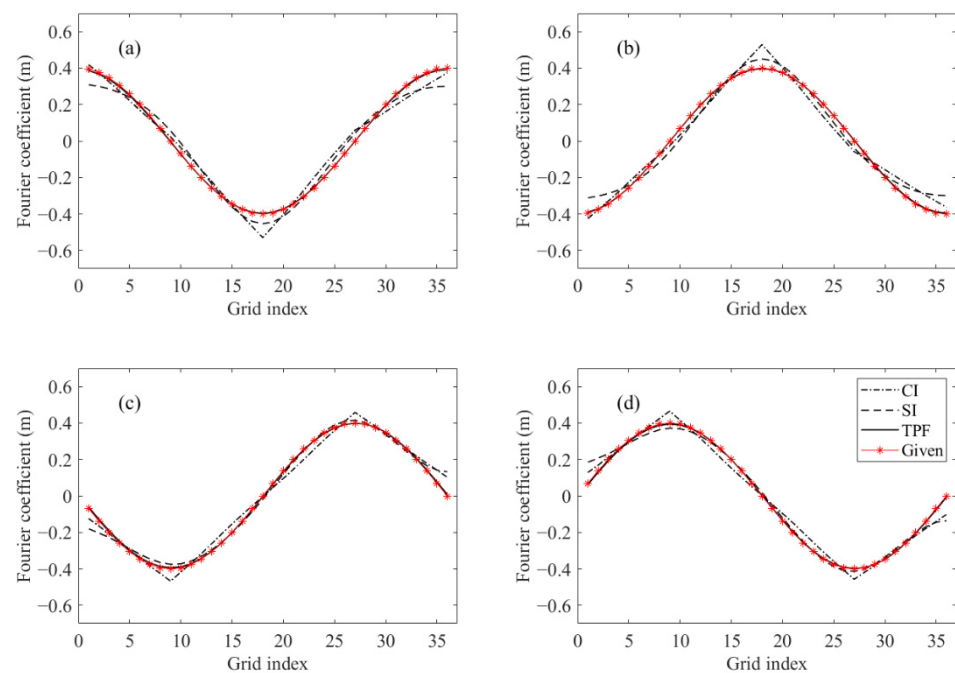


Figure 4. Given and inverted FCs α in TE-1 (a), TE-2 (b), TE-3 (c) and TE-4 (d).

In addition, many physical systems are impaired by some sort of noise. Considering factors including disturbance from the environment and precision of observation instruments, errors are inevitable in actual observations. In the simulation process, there will be approximation and truncation in the model as well. Therefore, TEs 5–8 are conducted to investigate the performance of different methods in the presence of errors. The Gaussian white noise is selected as the error and added into the time series of water elevations, and then OBCs are inverted by adjoint assimilation. Prescribed FCs are constructed from the characteristics of OBCs obtained by inversion in previous studies. The data with noise are generated as follows: the forward model is run with prescribed FCs α and β to obtain “observations”, and then Gaussian white noise is added to the “observations”. Noise–signal

power ratio (NSPR) is used as a measure of added white noise value. In TEs 5–8, Gaussian white noise with NSPR of 5%, 10%, 15% and 20% is added to the “observations”, respectively, and FCs α and β are inverted. The inversion process terminates when the number of iteration steps reaches 200. In TEs 5–8, for CI and SI schemes, seven independent points are selected uniformly, and the MTP in TPF scheme is set to 3. The given and inverted FCs are displayed in Figure 5.

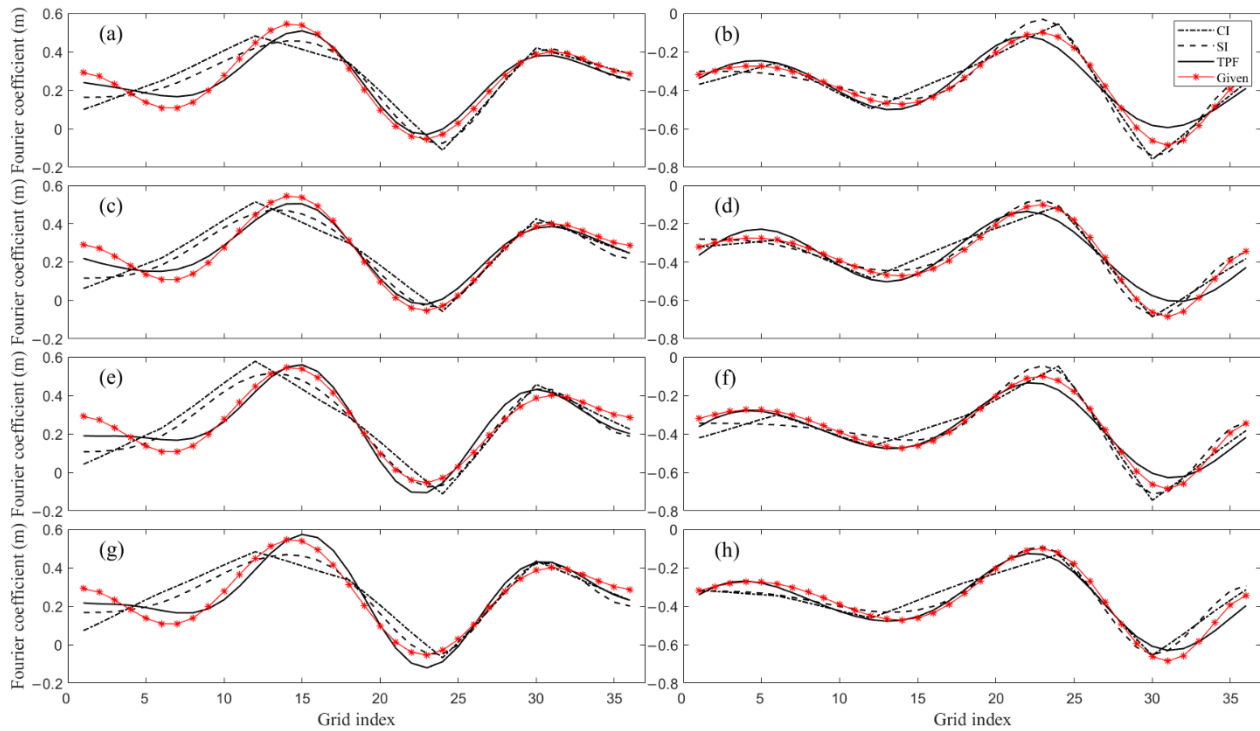


Figure 5. Given and inverted FCs of TE-5 α (a) and β (b), TE-6 α (c) and β (d), TE-7 α (e) and β (f), and TE-8 α (g) and β (h).

To quantitatively evaluate the results simulated with different methods, the root-mean-square (RMS) error between the simulated water elevations and the observations are calculated according to the following formulation [6,25,48]:

$$\text{RMS} = \left(\frac{1}{2D} \sum_{i=1}^D [\hat{A}_i \cos(\hat{P}_i) - A_i \cos(P_i)]^2 + [\hat{A}_i \sin(\hat{P}_i) - A_i \sin(P_i)]^2 \right)^{1/2} \quad (16)$$

where \hat{A}_i and \hat{P}_i are the observed tidal amplitudes and phases of the M_2 tidal constituent at the i th observation points, A_i and P_i are the corresponding simulated values and D is the number of observation points. Smaller RMS error means better consistency between simulated results and the observations.

3.3. Results and Discussion of TEs

The cost function describes the difference between the simulations and the observations, and its variation with the iteration steps shows the efficiency and stability of the inversion method. The decline in the cost function is described here by the normalized cost function (the ratio of the cost function to its initial value) in log form, which reduces significantly and stabilizes as the iteration step size increases (Figure 6). It should be noted that, under the influence of normalization, the normalized cost functions only show the decreasing trend and the extent of decrease, while the specific values that the differences can reduce to are reflected by the RMS errors. Correlation coefficients between the prescribed

and inverted FCs and RMS errors are calculated as quantitative indicators of the effect of different methods (Table 1).

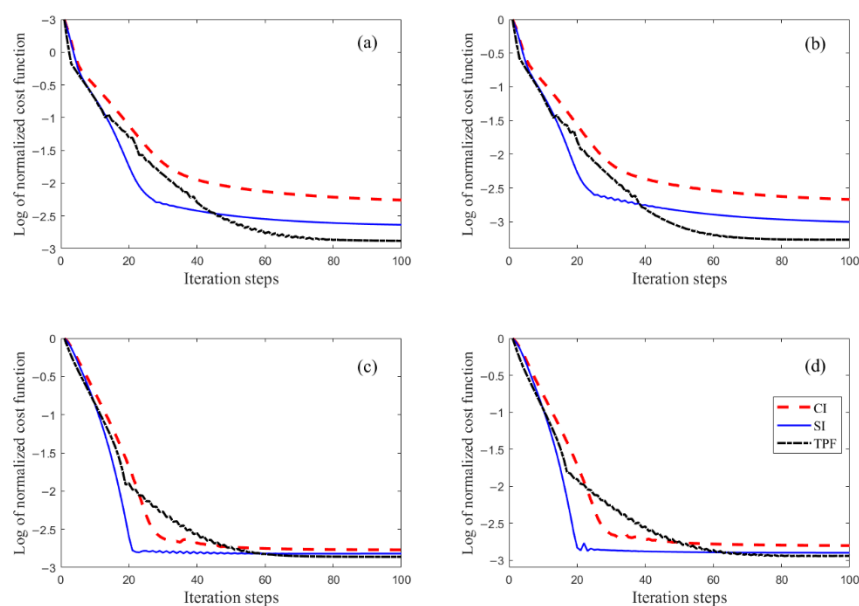


Figure 6. The descent process with iteration steps for the normalized cost function in log form of TE-1 (a), TE-2 (b), TE-3 (c) and TE-4 (d).

Table 1. RMS errors and correlation coefficients of TE 1–4.

TE	CI		SI		TPF	
	RMS (cm)	Correlation Coefficient	RMS (cm)	Correlation Coefficient	RMS (cm)	Correlation Coefficient
1	0.71	0.988	0.37	0.996	0.17	1.000
2	0.69	0.989	0.39	0.997	0.17	1.000
3	0.30	0.992	0.19	0.994	0.11	1.000
4	0.35	0.992	0.13	0.994	0.09	1.000

The prescribed FCs are successfully inverted by IPs schemes and TPF scheme (Figure 4); however, the inverted results obtained by TPF and SI scheme are smoother compared with CI scheme. The cost functions decrease to about 10^{-3} of their initial values; the cost function of SI scheme descends fastest, while the cost function of TPF scheme can be decreased to a lower level (Figure 6). Quantitatively, the RMS errors of TEs 1–2 are larger than those of TEs 3–4, and the RMS errors of TPF scheme are the lowest in different TEs, which are 0.17 cm, 0.17 cm, 0.11 cm and 0.09 cm, respectively (Table 1). The correlation coefficients of inverted and prescribed FCs in TEs 1–4 are all above 0.988. Although a lower RMS error does not guarantee a greater correlation coefficient, the correlation coefficients of TPF scheme in TEs 1–4 maintain at a large level (greater than 0.999). The inverted results and quantitative indicators of TEs 1–4 show that, in the ideal case, the TPF scheme has better performance compared with the IPs scheme in tidal OBCs estimation.

The FCs in TEs 5–8 are also inverted successfully (Figure 5), and the results of TPF scheme are more consistent with the prescribed FCs. A control experiment without adding white noise is conducted, and the inverted FCs and normalized cost functions are shown in Figure 7. The descent process of cost functions in different experiments (Figure 8) shows that, with the increase in NSPR, the extent of decrease in cost functions becomes smaller. In contrast to the previous situation, when there exist observation errors, the cost function of the TPF scheme descends faster compared to that of the IPs scheme. The normalized cost function of TPF scheme is the lowest, except in TE-7 (Figure 8b); however, TE-7 is

the experiment with the least difference in normalized cost function by different methods (about 10^{-4} orders of magnitude, while other TEs are about 10^{-3}).

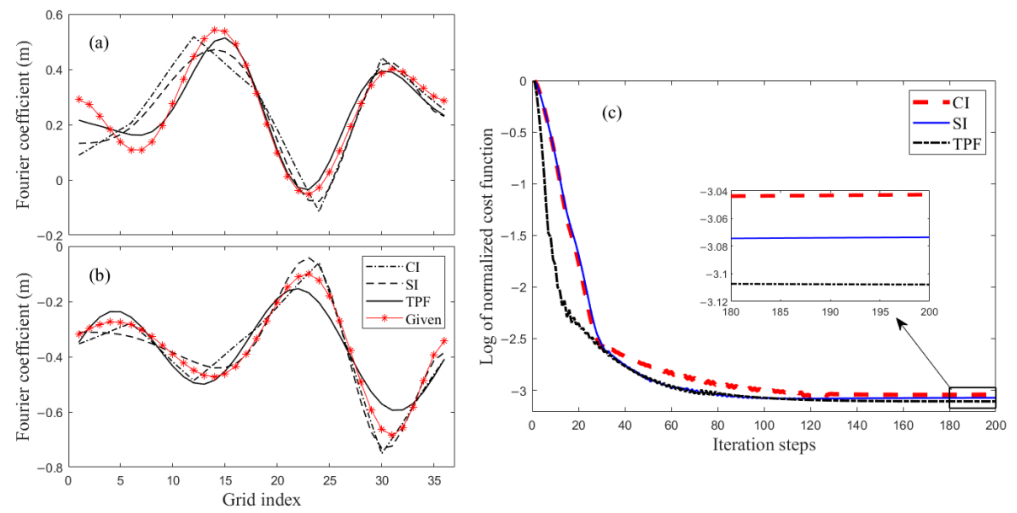


Figure 7. Prescribed and inverted FCs α (a) and β (b) and the descent process with iteration steps for the normalized cost function (c) of control experiment.

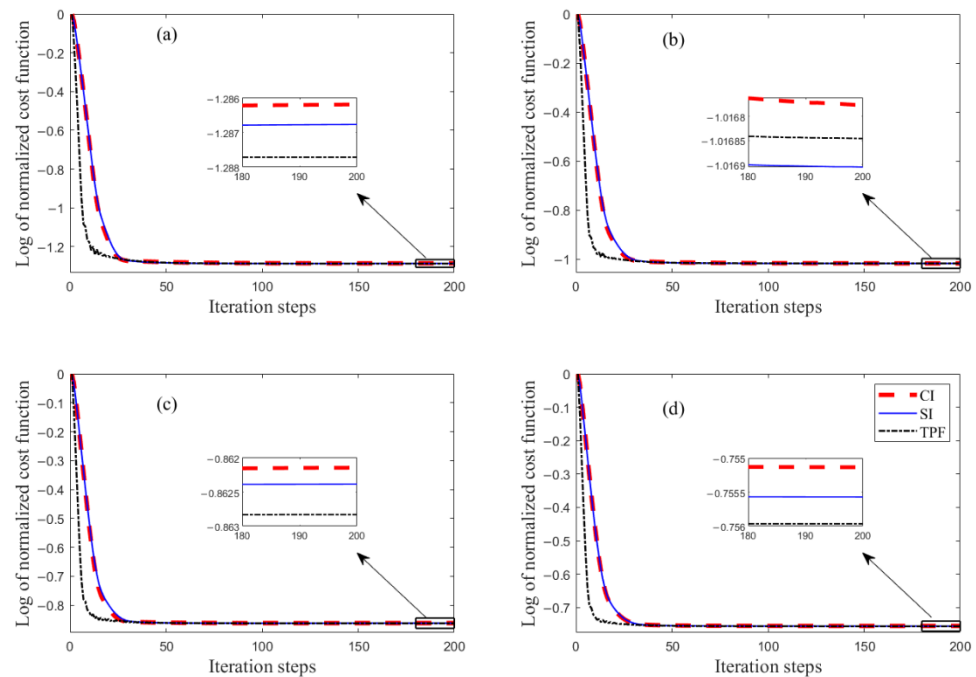


Figure 8. The descent process with iteration steps for the normalized cost function in log form of TE-5 (a), TE-6 (b), TE-7 (c) and TE-8 (d).

It can be obtained from Table 2 that, as the NSPR increases, the RMS error also increases, which is shown visually in Figure 9. By comparison, with the same NSPR used, the RMS error of TPF scheme is the smallest, only 4.8 cm at 20% NSPR, which is better than most results of IPs scheme. The correlation coefficients of β obtained by IPs scheme are slightly higher than those of α , while those of FCs obtained by TPF scheme are closer. The correlation between FCs inverted by TPF scheme and prescribed is better, with all of the coefficients >0.95 , which is the best among all approaches. Similar to the results of TEs 1–4, the correlation coefficients are not monotonously decreased with the RMS error. With the increase in NSPR, the correlation coefficients generally show a decreasing trend. The addition of Gaussian white noise does have a negative effect on the inversion. For both

IPs scheme and TPF scheme, the higher noise power is, the worse inversion results will be. Compared with CI and SI scheme, TPF scheme is obviously less affected (Figure 9), indicating its better stability.

Table 2. RMS errors and correlation coefficients of TE 5–8.

NSPR	CI			SI			TPF		
	RMS (cm)	Correlation Coefficient		RMS (cm)	Correlation Coefficient		RMS (cm)	Correlation Coefficient	
		α	β		α	β		α	β
0%	0.63	0.852	0.970	0.44	0.916	0.982	0.32	0.979	0.953
5%	0.67	0.836	0.971	0.47	0.919	0.980	0.37	0.986	0.966
10%	0.70	0.817	0.968	0.51	0.899	0.984	0.39	0.985	0.952
15%	0.86	0.809	0.954	0.68	0.887	0.967	0.44	0.961	0.981
20%	0.94	0.799	0.943	0.72	0.907	0.960	0.48	0.968	0.983

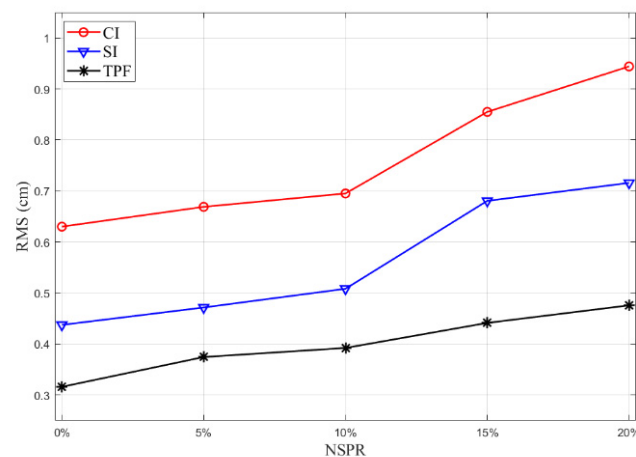


Figure 9. Variation in RMS with NSPR in TEs 5–8.

In the TEs, OBCs are estimated and water elevations are simulated by assimilating “observations” using different approaches. According to the results of TEs, the FCs inverted by TPF scheme are smoother and closer to the given distribution compared with IPs scheme (Figures 3 and 4). In TEs 1–4, quantitative indicators also show that the TPF scheme performs better, the RMS errors of simulation are smaller and correlation coefficients between inverted and given are larger (Tables 1 and 2). In TEs 5–8, white noise of different NSPR is added, and the estimation and simulations of the TPF scheme are less affected by errors, which reflects its better stability. However, the effectiveness of the TPF scheme is affected, as the error in the observed data increases, which means that the scheme is still dependent on the accuracy of the observed data.

4. Practical Experiments

In this section, the TPF scheme is applied to an actual situation. The OBCs of BYS are inverted by assimilating T/P-Jason altimeter data processed by X-TRACK to realize the numerical simulation of the M_2 tidal constituent. The inversion process terminates when the number of iteration steps reaches 100.

4.1. Selection of MTP in TPF Scheme

In order to optimize the estimation, experiments are constructed on the MTP of TPF scheme in the BYS simulation domain with $1/6^\circ$ horizontal resolution. The MTP is set as 2, 3, 4, 5, 6, 7 and 8, respectively, and the FCs of M_2 tidal OBCs are inverted (Figure 10). The mean absolute errors (MAE) of the harmonic constants obtained by simulations and

altimeter data are calculated. In the computing of RMS errors, data from 22 tidal gauges (Figure 1, red points) in the computation domain are included for further verification (Table 3).

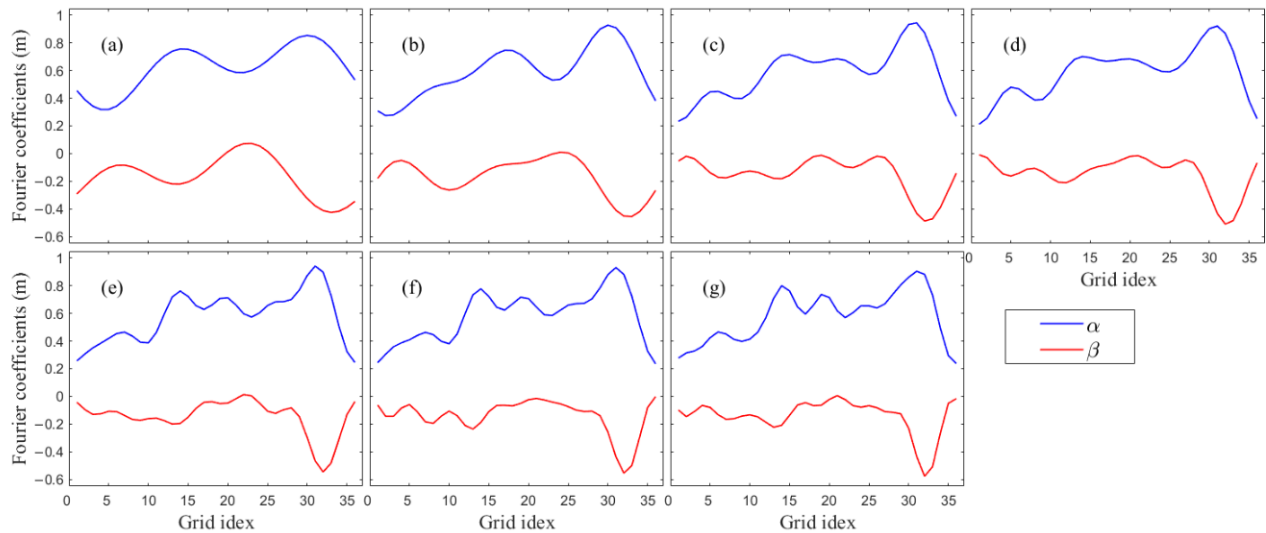


Figure 10. FCs inverted by assimilating T/P-Jason data with MTP of 2 (a), 3 (b), 4 (c), 5 (d), 6 (e), 7 (f), 8 (g).

Table 3. MAE and RMS errors between simulation and observations in the practical experiment.

MTP	MAE		RMS (cm)	
	Amplitude (cm)	Phase (°)	T/P-Jason	Tidal Gauges
2	2.83	2.32	3.75	7.70
3	2.82	2.26	3.69	7.70
4	2.81	2.28	3.69	7.75
5	2.79	2.29	3.68	7.73
6	2.79	2.29	3.68	7.81
7	2.79	2.29	3.68	7.78
8	2.79	2.28	3.68	7.77

The FCs inverted with different MTP show similar spatial characteristics. The error between simulation and altimeter data is the largest when MTP is 2. As the MTP increases, the error between simulated values and altimeter data decreases; however, when MTP is greater than 4, the errors do not change significantly. Figure 10 shows that inverse FCs may be overfitted when the MTP is greater than 5 due to the horizontal resolution limitation, which is manifested by the appearance of too many extreme value points. It can also be obtained from Table 3 that the errors between simulation and tidal gauge data increase when the MTP is too large (>3).

4.2. Validation of the Model

The M_2 tidal constituent harmonic constants of BYS are derived from TPXO9, FES2014, EOT20, NAO.99b and OSU12, respectively. The FCs of harmonic constants from model data are calculated on the open boundary of the simulation domain (Figure 11). The forward model is driven with the FCs derived from tide models to obtain the simulations in the computation domain. Quantitatively, the simulation results are compared with the observations (Table 4).

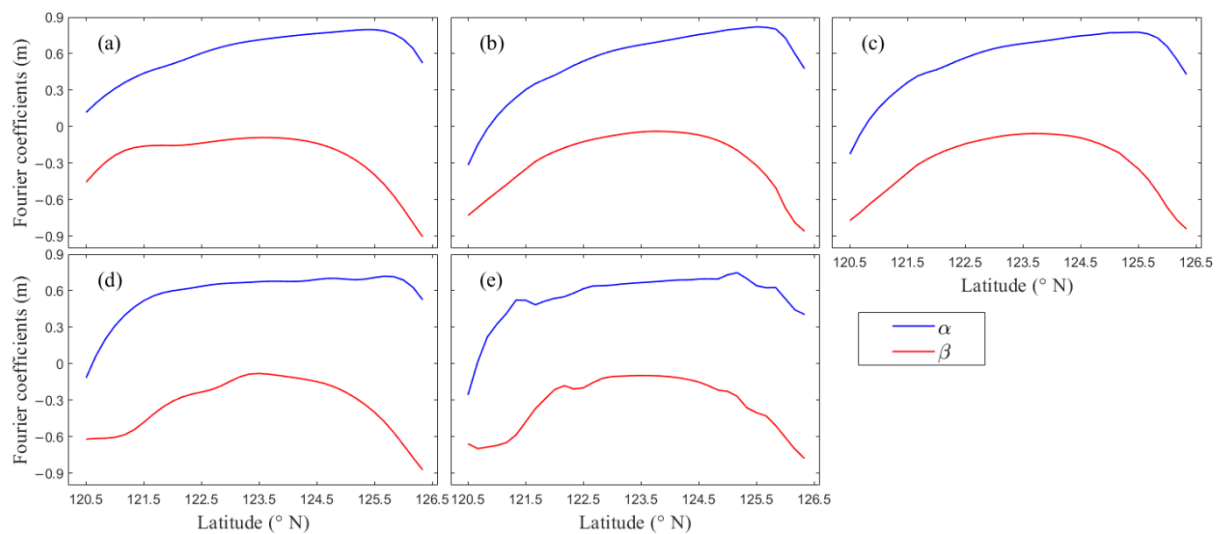


Figure 11. FCs of OBCs derived from model data TPXO9 (a), FES2014 (b), EOT20 (c), NAO.99b (d) and OSU12 (e).

Table 4. RMS errors between observations and simulations with OBCs derived from large-scale tidal models.

Model	RMS (cm)	
	T/P-Jason	Tidal Gauges
TPXO9	6.09	11.83
FES2014	8.48	9.01
EOT20	7.67	9.97
NAO.99b	11.66	17.76
OSU12	11.38	16.98

Table 4 indicates that the differences between simulations using OBCs obtained from TPXO9 and T/P-Jason data are the smallest, with the RMS error of 6.09 cm. When compared with the tidal gauge data, simulations using OBCs obtained from FES2014 are more advantageous, with the RMS error of 9.01 cm. However, simulation results using the OBCs derived from these model data have greater difference from the observations than those obtained through data assimilation (Table 3). Moreover, when the resolution of the model used is different from the data, it is still necessary to preprocess the data by interpolating or fitting the data, which may cause errors. Therefore, in practical applications, the use of concomitant assimilation methods to estimate tidal OBCs is beneficial to improve the accuracy of tidal simulation.

Harmonic constants of hydrodynamic models (TPXO9, FES2014 and NAO.99b) in BYS are directly obtained to further verify the effectiveness of the TPF scheme. These models assimilate altimeter data; it is more representative to use tide gauge data for comparison (Table 5). The performance of FES2014 on the coast is much better than the other two models, with the RMS error of 8.73 cm. FES2014 has the highest horizontal resolution. In addition to model algorithm and assimilation methods, errors may be affected by horizontal resolution. However, according to Table 3, the RMS errors between the simulation results obtained by TPF scheme and the tide gauge data are still lower than that of the hydrodynamic model data, which indicates the superiority of this scheme.

Table 5. RMS errors between tide gauge data and model data.

Model	TPXO9	FES2014	NAO.99b
RMS (cm)	17.92	8.73	25.13

4.3. Comparison of Different Approaches

The FCs along the OBCs are inverted by the IPs scheme and the M_2 tidal constituent is simulated for the computation domain; seven independent points are selected uniformly. The estimated and simulated values were used to compare with the results corresponding to the TPF scheme at MTP = 3. The inverted FCs and the descent process of cost functions are shown in Figure 12. The normalized cost functions of different approaches all decreased below 0.004; however, the cost function of TPF scheme is lower and the decline process is more rapid (Figure 12c).

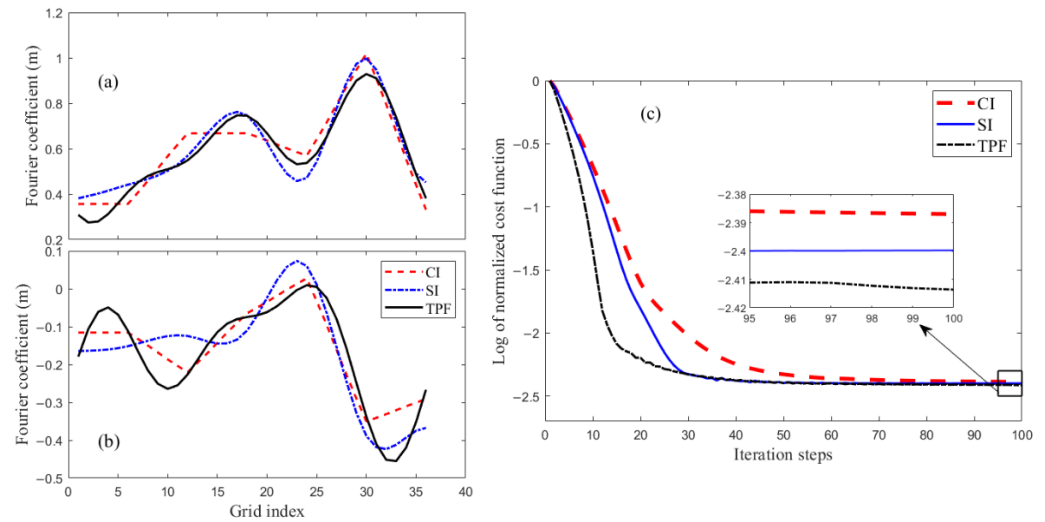


Figure 12. FCs α (a) and β (b) and the descent process with iteration steps for the normalized cost function (c) inverted by different approaches.

The RMS errors of the harmonic constants obtained by simulation and observation (both T/P-Jason and tidal gauges data) are calculated (Table 6). The simulation results obtained from the TPF scheme have RMS errors of 3.69 cm and 7.70 cm for TP-Jason data and tide gauge data, respectively, which are the smallest among the results of the three schemes. Compared with altimeter data, the differences between the simulated results and tidal gauge data are larger.

Table 6. RMS errors between observations and simulations obtained by different approaches.

	CI	SI	TPF
T/P-Jason (cm)	3.80	3.73	3.69
Tidal Gauge (cm)	8.07	7.97	7.70

The magnitude of misfit vector is calculated to compare the difference of tidal harmonic constants at each grid point between observation and simulation results of different approaches, and it is expressed as:

$$\Delta r = \frac{1}{2} \left\{ \left[A \cos(P) - \tilde{A} \cos(\tilde{P}) \right]^2 + \left[A \sin(P) - \tilde{A} \sin(\tilde{P}) \right]^2 \right\}^{1/2} \quad (17)$$

where Δr represents misfit vector, A and \tilde{A} are the amplitudes for comparison, and P and \tilde{P} are the corresponding phase lags.

The magnitude of misfit vector between the simulated results and tidal gauge observations is shown in Figure 13. On more than half of the computational grids where the tidal gauges are located, the magnitude of misfit vector presents TPF scheme as the smallest, followed by SI scheme, and CI scheme as the largest.

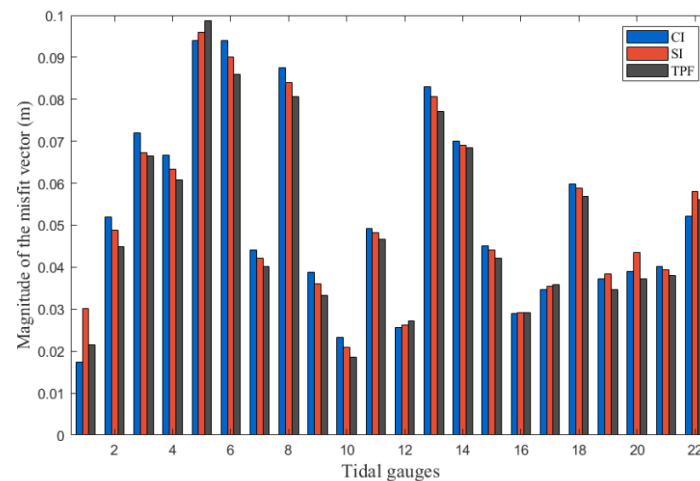


Figure 13. Magnitude of the misfit vector between the simulations and each tidal gauge.

4.4. Discussion

The M_2 tidal OBCs in the BYS simulation domain with $1/6^\circ$ horizontal resolution are estimated using the TPF scheme. After numerous experiments, 3 is considered to be the optimal value of MTP in this computation domain. The inversion results with SI and CI were also compared. The differences between simulation and observation show that the TPF scheme performs better both with altimeter data and tide gauge station data.

Based on the OBCs estimated via assimilating T/P-Jason records using TPF scheme, M_2 cotidal charts in the BYS are derived, as shown in Figure 14. The cotidal chart shows the following characteristics: greater amplitude on the west side compared to the east side, with a maximum amplitude of more than 3 m; and there are four amphidromic points in the whole area, among which there are two in the Bohai Sea, they are closer to the shore, located near Qinhuangdao and the Yellow River Delta, and the two in the Yellow Sea are farther offshore and more obvious, located in the north of Chengshantou and the vicinity Jiangsu. In addition, the M_2 cotidal chart coincides fairly well with those in previous research [20,49,50] in the BYS. Supplementary experiments are constructed. In the gulf of Thailand simulation domain with $1/6^\circ$ horizontal resolution, the OBCs of K_1 tidal constituent are estimated by using TPF scheme, and satisfactory results are also obtained. In addition, the OBCs of S_2 , K_1 and O_1 tidal constituents in the BYS are estimated and corresponding cotidal charts are drawn. Details can be seen in the supplementary material.

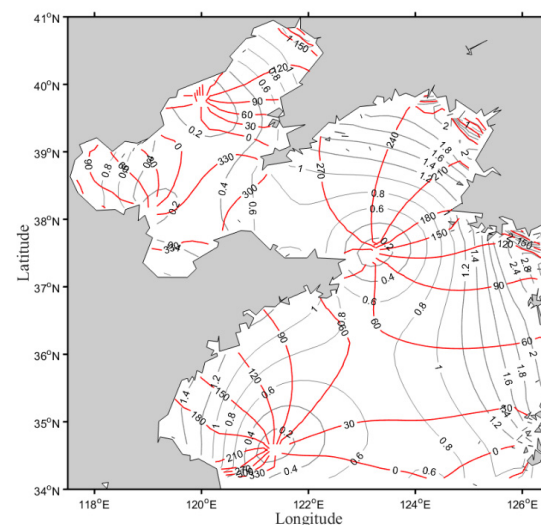


Figure 14. Cotidal chart for the M_2 constituent in the BYS obtained by TPF scheme. Gray line denotes the co-amplitude line (m), red line denotes the co-phase line ($^\circ$).

5. Conclusions

In this paper, TPF is developed to improve a 2D tidal model and the OBCs of M_2 tide are estimated via assimilating altimeter data. The FCs of OBCs are expressed in the form of a discrete Fourier series and the coefficients of trigonometric polynomials are taken as control parameters. The adjoint method is applied to correct the coefficients of trigonometric polynomials to optimize the OBCs.

The M_2 constituent is simulated by applying prescribed OBCs, the simulation results on altimeter tracks are selected as “observations” and a series of TEs are constructed by assimilating the “observations”. Considering the actual and model errors, white noise of different NSPR was added into the “observed value” in some twin experiments. The TPF scheme is calibrated and the OBCs are successfully inverted by TPF scheme in TEs. Compared with the IPs scheme, the OBCs obtained by TPF maintain smoothness and are closer to the prescribed distribution, with smaller RMS errors and better stability. In the BYS simulation domain with $1/6^\circ$ horizontal resolution, T/P-Jason data are assimilated to estimate the OBCs for the M_2 tidal constituent. The tidal gauge data are also included to verify the effectiveness of the simulation. The quantitative indicators show that the TPF scheme has a better performance in this simulation domain while MTP is 3. Tidal data derived from TPXO9, FES2014, EOT20, NAO.99b and OSU12 are taken into consideration, which are used to obtain OBCs in the computation domain to verify the performance of TPF scheme. Moreover, compared to the SI and CI schemes, the simulation results of the TPF scheme agree better with the observed data. The cotidal chart simulated with TPF scheme accurately reflects the characteristics of M_2 constituent in the BYS.

In conclusion, the TPF scheme is an effective improvement in the estimation of the OBCs in tidal models. However, its effectiveness in use still depends largely on data quantity and accuracy. Supported by observations, TPF scheme can provide more accurate tidal OBCs for the marginal ocean tidal model. In future research, the TPF method can be combined with the estimation of BFCs, eddy viscosity profiles and other parameters in the tidal model and achieve a more accurate simulation of regional tides.

Supplementary Materials: The following supporting information can be downloaded at: <https://www.mdpi.com/article/10.3390/rs15020480/s1>, Figure S1: (a) The bathymetry (unit: m), open boundaries (red circles) and the T/P-Jason altimeter tracks. (b) The spatially varying BFCs of the Gulf of Thailand; Figure S2: The amplitude (a) and phase (b) of K1 constituent along T/P-Jason altimeter tracks in the Gulf of Thailand; Figure S3: FCs (a) and the descent process with iteration steps for the normalized cost function (b) inverted by TPF scheme; Figure S4: FCs of OBCs derived from model data TPXO9 (a), FES2014 (b), and EOT20 (c); Figure S5: Cotidal chart for the K1 constituent in the Gulf of Thailand obtained TPF scheme. Gray line denotes the co-amplitude line (m), red line denotes the co-phase line ($^\circ$); Figure S6: Inverted FCs of S2 (a), K1 (b) and O1 (c) tidal constituents; Figure S7: Cotidal chart for the S2 constituent in the BYS obtained TPF scheme. Gray line denotes the co-amplitude line (m), red line denotes the co-phase line ($^\circ$); Figure S8: Similar to Figure S7, but for K1 constituent; Figure S9: Similar to Figure S7, but for O1 constituent; Table S1: MAE and RMS errors between simulation and observations; Table S2: MAE and RMS errors between simulation and observations of different tidal constituents.

Author Contributions: Conceptualization, X.L. and H.P.; methodology, X.L. and S.J.; software, S.J. and X.L.; validation, S.J.; formal analysis, S.J. and Y.Z.; investigation, S.J.; writing—original draft preparation, S.J. and Y.Z.; writing—review and editing, S.J., Y.Z. and H.P.; visualization, S.J.; supervision, X.L. and H.P. All authors have read and agreed to the published version of the manuscript.

Funding: This research is jointly supported by the National Natural Science Foundation of China (No. 42206022, 42076011 and U1806214), the Natural Science Foundation of Shandong Province of China (No. ZR2020MD056), the National Key Research and Development Project of China (No. 2019YFC140840), China Postdoctoral Science Foundation (2022M713677) and Qingdao postdoctoral application research project (QDBSH202108).

Data Availability Statement: The regional along-track sea level anomaly data T/P-Jason altimeters are obtained from AVISO (<https://www.aviso.altimetry.fr/en/data/products/auxiliary-products/coastal-tide-xtrack.html>), accessed on 15 November 2021. The tidal data from TPXO9 are available at volkov.oce.orst.edu/tides/tpxo9_atlas.html, accessed on 8 March 2018. The tidal data from FES2014 are available at <https://www.aviso.altimetry.fr/en/data/products/auxiliary-products/global-tide-fes/description-fes2014.html>, accessed on 7 December 2017. The tidal data from EOT20 are available at <https://doi.org/10.17882/79489>, accessed on 25 June 2021.

Conflicts of Interest: The authors declare no conflict of interest.

References

- Doodson, A.T. The harmonic development of the tide-generating potential. *Proc. R. Soc. Lond. A* **1921**, *100*, 305–329. [[CrossRef](#)]
- Munk, W. Once again: Once again-Tidal friction. *Prog. Oceanogr.* **1997**, *40*, 7–35. [[CrossRef](#)]
- Fang, G. Tide and tidal current charts for the marginal seas adjacent to China. *Chin. J. Oceanol. Limnol.* **1986**, *4*, 1–16. [[CrossRef](#)]
- Kang, S.K.; Lee, S.-R.; Lie, H.-J. Fine grid tidal modeling of the Yellow and East China Seas. *Cont. Shelf Res.* **1998**, *18*, 739–772. [[CrossRef](#)]
- Lefevre, F.; Le Provost, C.; Lyard, F.H. How can we improve a global ocean tide model at a regional scale? A test on the Yellow Sea and the East China Sea. *J. Geophys. Res.* **2000**, *105*, 8707–8725. [[CrossRef](#)]
- Zheng, J.; Mao, X.; Lv, X.; Jiang, W. The m2 cotidal chart in the bohai, yellow, and east china seas from dynamically constrained interpolation. *J. Atmos. Ocean. Technol.* **2020**, *37*, 1219–1229. [[CrossRef](#)]
- Chapman, D.C. Numerical treatment of cross-shelf open boundaries in a barotropic coastal ocean model. *J. Phys. Ocean.* **1985**, *15*, 1060–1075. [[CrossRef](#)]
- Zhang, A.; Wei, E.; Parker, B.B. Optimal estimation of tidal open boundary conditions using predicted tides and adjoint data assimilation technique. *Cont. Shelf Res.* **2003**, *23*, 1055–1070. [[CrossRef](#)]
- Egbert, G.D. Tidal data inversion: Interpolation and inference. *Prog. Oceanogr.* **1997**, *40*, 53–80. [[CrossRef](#)]
- Egbert, G.D.; Erofeeva, S.Y. Efficient inverse modeling of barotropic ocean tides. *J. Atmos. Ocean. Technol.* **2002**, *19*, 183–204. [[CrossRef](#)]
- Lardner, R.W. Optimal control of open boundary conditions for a numerical tidal model. *Comput. Methods Appl. Mech. Eng.* **1993**, *102*, 367–387. [[CrossRef](#)]
- Cheng, Y.; Andersen, O.B. Multimission empirical ocean tide modeling for shallow waters and polar seas. *J. Geophys. Res. Ocean.* **2011**, *116*, 1–11. [[CrossRef](#)]
- Bennett, A.F.; McIntosh, P.C. Open Ocean Modeling as an Inverse Problem: Tidal Theory. *J. Phys. Oceanogr.* **1982**, *12*, 1004–1018. [[CrossRef](#)]
- Seiler, U. Estimation of open boundary conditions with the adjoint method. *J. Geophys. Res.* **1993**, *98*, 22855–22870. [[CrossRef](#)]
- Lardner, R.W.; Al-Rabeh, A.H.; Gunay, N. Optimal estimation of parameters for a two-dimensional hydrodynamical model of the Arabian gulf. *J. Geophys. Res.* **1993**, *98*, 229–242. [[CrossRef](#)]
- Heemink, A.W.; Mouthaan, E.E.A.; Roest, M.R.T.; Vollebregt, E.A.H.; Robaczewska, K.B.; Verlaan, M. Inverse 3D shallow water flow modelling of the continental shelf. *Cont. Shelf Res.* **2002**, *22*, 465–484. [[CrossRef](#)]
- Zhang, A.; Parker, B.B.; Wei, E. Assimilation of water level data into a coastal hydrodynamic model by an adjoint optimal technique. *Cont. Shelf Res.* **2002**, *22*, 1909–1934. [[CrossRef](#)]
- Zhang, J.; Lu, X. Inversion of three-dimensional tidal currents in marginal seas by assimilating satellite altimetry. *Comput. Methods Appl. Mech. Eng.* **2010**, *199*, 3125–3136. [[CrossRef](#)]
- Adebisi, N.; Balogun, A.L.; Min, T.H.; Tella, A. Advances in estimating Sea Level Rise: A review of tide gauge, satellite altimetry and spatial data science approaches. *Ocean Coast. Manag.* **2021**, *208*, 105632. [[CrossRef](#)]
- Fang, G.; Wang, Y.; Wei, Z.; Choi, B.H.; Wang, X.; Wang, J. Empirical cotidal charts of the Bohai, Yellow, and East China Seas from 10 years of TOPEX/Poseidon altimetry. *J. Geophys. Res. Ocean.* **2004**, *109*, 1–13. [[CrossRef](#)]
- Teague, W.J.; Pistek, P.; Jacobs, G.A.; Perkins, H.T. Evaluation of tides from TOPEX/Poseidon in the Bohai and Yellow Seas. *J. Atmos. Ocean. Technol.* **2000**, *17*, 679–687. [[CrossRef](#)]
- Birol, F.; Fuller, N.; Lyard, F.; Cancet, M.; Niño, F.; Delebecque, C.; Fleury, S.; Toubanc, F.; Melet, A.; Saraceno, M.; et al. Coastal applications from nadir altimetry: Example of the X-TRACK regional products. *Adv. Sp. Res.* **2017**, *59*, 936–953. [[CrossRef](#)]
- Fok, H.S. Ocean Tides Modeling Using Satellite Altimetry. Ph.D. Thesis, Ohio State University, Columbus, OH, USA, 2012.
- Marcos, M.; Wöppelmann, G.; Matthews, A.; Ponte, R.M.; Birol, F.; Arduin, F.; Coco, G.; Santamaría-Gómez, A.; Ballu, V.; Testut, L.; et al. Coastal Sea Level and Related Fields from Existing Observing Systems. *Surv. Geophys.* **2019**, *40*, 1293–1317. [[CrossRef](#)]
- Stammer, D.; Ray, R.D.; Andersen, O.B.; Arbic, B.K.; Bosch, W.; Carrère, L.; Cheng, Y.; Chinn, D.S.; Dushaw, B.D.; Egbert, G.D.; et al. Accuracy assessment of global barotropic ocean tide models. *Rev. Geophys.* **2014**, *52*, 243–282. [[CrossRef](#)]
- Save, H.; Bettadpur, S.; Tapley, B.D. High-resolution CSR GRACE RL05 mascons. *J. Geophys. Res. Solid Earth.* **2016**, *121*, 7547–7569. [[CrossRef](#)]
- Smedstad, O.M.; O'Brien, J.J. Variational data assimilation and parameter estimation in an equatorial Pacific ocean model. *Prog. Oceanogr.* **1991**, *26*, 179–241. [[CrossRef](#)]

28. Chertok, D.L.; Lardner, R.W. Variational data assimilation for a nonlinear hydraulic model. *Appl. Math. Model.* **1996**, *20*, 675–682. [[CrossRef](#)]
29. Navon, I.M. Practical and theoretical aspects of adjoint parameter estimation and identifiability in meteorology and oceanography. *Dyn. Atmos. Ocean.* **1998**, *27*, 55–79. [[CrossRef](#)]
30. Lu, X.; Zhang, J. Numerical study on spatially varying bottom friction coefficient of a 2D tidal model with adjoint method. *Cont. Shelf Res.* **2006**, *26*, 1905–1923. [[CrossRef](#)]
31. Cao, A.; Guo, Z.; Lü, X. Inversion of two-dimensional tidal open boundary conditions of M2 constituent in the Bohai and Yellow Seas. *Chin. J. Oceanol. Limnol.* **2012**, *30*, 868–875. [[CrossRef](#)]
32. Guo, Z.; Cao, A.; Lv, X. Inverse estimation of open boundary conditions in the Bohai Sea. *Math. Probl. Eng.* **2012**, *34*, 2021–2028. [[CrossRef](#)]
33. Chen, H.; Cao, A.; Zhang, J.; Miao, C.; Lv, X. Estimation of spatially varying open boundary conditions for a numerical internal tidal model with adjoint method. *Math. Comput. Simul.* **2014**, *97*, 14–38. [[CrossRef](#)]
34. Gao, Y.; Cao, A.; Chen, H.; Lv, X. Estimation of bottom friction coefficients based on an isopycnic-coordinate internal tidal model with adjoint method. *Math. Probl. Eng.* **2013**, *2013*, 532814. [[CrossRef](#)]
35. Zhang, J.; Wang, Y.P. A method for inversion of periodic open boundary conditions in two-dimensional tidal models. *Comput. Methods Appl. Mech. Eng.* **2014**, *275*, 20–38. [[CrossRef](#)]
36. Pan, H.; Guo, Z.; Lv, X. Inversion of tidal open boundary conditions of the M2 constituent in the bohai and yellow seas. *J. Atmos. Ocean. Technol.* **2017**, *34*, 1661–1672. [[CrossRef](#)]
37. Guo, Z.; Pan, H.; Fan, W.; Lv, X. Application of surface spline interpolation in inversion of bottom friction coefficients. *J. Atmos. Ocean. Technol.* **2017**, *34*, 2021–2028. [[CrossRef](#)]
38. Jiang, D.; Chen, H.; Jin, G.; Lv, X. Estimating smoothly varying open boundary conditions for a 3D internal tidal model with an improved independent point scheme. *J. Atmos. Ocean. Technol.* **2018**, *35*, 1299–1311. [[CrossRef](#)]
39. Wahr, J.M. Body tides on an elliptical, rotating, elastic and oceanless earth. *Geophys. J. R. Astron. Soc.* **1981**, *64*, 677–703. [[CrossRef](#)]
40. Zhang, J.C.; Lu, X.Q. Parameter estimation for a three-dimensional numerical barotropic tidal model with adjoint method. *Int. J. Numer. Methods Fluids* **2008**, *57*, 47–92. [[CrossRef](#)]
41. Egbert, G.D.; Bennett, A.F.; Foreman, M.G.G. TOPEX/POSEIDON tides estimated using a global inverse model. *J. Geophys. Res.* **1994**, *99*, 24821–24852. [[CrossRef](#)]
42. Carrere, L.; Lyard, F.; Cancet, M.; Guillot, A. FES 2014, a new tidal model on the global ocean with enhanced accuracy in shallow seas and in the Arctic region. In Proceedings of the EGU General Assembly Conference Abstracts, Vienna, Austria, 12–17 April 2015. Abstract 5481.
43. Hart-Davis, M.G.; Piccioni, G.; Dettmering, D.; Schwatke, C.; Passaro, M.; Seitz, F. EOT20: A global ocean tide model from multi-mission satellite altimetry. *Earth Syst. Sci. Data* **2021**, *13*, 3869–3884. [[CrossRef](#)]
44. Matsumoto, K.; Takanezawa, T.; Ooe, M. Ocean Tide Models Developed by Assimilating TOPEX/POSEIDON Altimeter Data into Hydrodynamical Model: A Global Model and a Regional Model around Japan. *J. Oceanogr.* **2000**, *56*, 567–581. [[CrossRef](#)]
45. Edwards, K.A.; MacCready, P.; Moum, J.N.; Pawlak, G.; Klymak, J.M.; Perlin, A. Form drag and mixing due to tidal flow past a sharp point. *J. Phys. Oceanogr.* **2004**, *34*, 1297–1312. [[CrossRef](#)]
46. Bo, T.; Ralston, D.K. Flow Separation and Increased Drag Coefficient in Estuarine Channels with Curvature. *J. Geophys. Res. Ocean.* **2020**, *125*, 1–25. [[CrossRef](#)]
47. Wang, D.; Zhang, J.; Mu, L. A feature point scheme for improving estimation of the temporally varying bottom friction coefficient in tidal models using adjoint method. *Ocean Eng.* **2021**, *220*, 108481. [[CrossRef](#)]
48. King, M.A.; Padman, L. Accuracy assessment of ocean tide models around Antarctica. *Geophys. Res. Lett.* **2005**, *32*, 1–4. [[CrossRef](#)]
49. Wang, D.; Zhang, J.; Wang, Y.P. Estimation of Bottom Friction Coefficient in Multi-Constituent Tidal Models Using the Adjoint Method: Temporal Variations and Spatial Distributions. *J. Geophys. Res. Ocean.* **2021**, *126*, 1–20. [[CrossRef](#)]
50. Pan, H.; Jiao, S.; Xu, T.; Lv, X.; Wei, Z. Investigation of tidal evolution in the Bohai Sea using the combination of satellite altimeter records and numerical models. *Estuar. Coast. Shelf Sci.* **2022**, *279*, 108140. [[CrossRef](#)]

Disclaimer/Publisher's Note: The statements, opinions and data contained in all publications are solely those of the individual author(s) and contributor(s) and not of MDPI and/or the editor(s). MDPI and/or the editor(s) disclaim responsibility for any injury to people or property resulting from any ideas, methods, instructions or products referred to in the content.